# Pore-scale statistics of flow and transport through porous media

Soroush Aramideh, Pavlos P. Vlachos, and Arezoo M. Ardekani
*School of Mechanical Engineering, Purdue University, 585 Purdue Mall, West Lafayette, Indiana 47907, United States*

(Received 27 April 2018; published 13 July 2018)

Flow in porous media is known to be largely affected by pore morphology. In this work, we investigate the effects of pore geometry on the transport and spatial correlations of flow through porous media in two distinct pore structures arising from three-dimensional assemblies of overlapping and nonoverlapping spheres. Using high-resolution direct numerical simulations (DNS), we perform Eulerian and Lagrangian analysis of the flow and transport characteristics in porous media. We show that the Eulerian velocity distributions change from nearly exponential to Gaussian distributions as porosity increases. A stretched exponential distribution can be used to represent this behavior for a wide range of porosities. Evolution of Lagrangian velocities is studied for the uniform injection rule. Evaluation of tortuosity and trajectory length distributions of each porous medium shows that the model of overlapping spheres results in higher tortuosity and more skewed trajectory length distributions compared to the model of nonoverlapping spheres. Wider velocity distribution and higher tortuosity for overlapping spheres model give rise to non-Fickian transport while transport in nonoverlapping spheres model is found to be Fickian. Particularly, for overlapping spheres model our analysis of first-passage time distribution shows that the transport is very similar to those observed for sandstone. Finally, using three-dimensional (3D) velocity field obtained by DNS at the pore-scale, we quantitatively show that despite the randomness of pore-space, the spatially fluctuating velocity field and the 3D pore-space distribution are strongly correlated for a range of porous media from relatively homogeneous monodisperse sphere packs to Castlegate sandstone.

DOI: 10.1103/PhysRevE.98.013104

## I. INTRODUCTION

Understanding the flow through porous media is of great importance in many natural and technological processes such as oil recovery [1], $CO_2$ sequestration [2], filtration [3], biological flows [4], and reactive transport [5]. In many practical cases, low Reynolds number flows through porous media are modeled at the Darcy scale using Darcy's law, which relates the specific discharge, $q$, to the pressure drop, $\Delta p$, along the flow direction as

$$q = \frac{-\kappa}{\mu}\frac{\Delta p}{L}, \tag{1}$$

where $\kappa$ is the permeability, $\mu$ is the viscosity of the fluid, and $L$ is the length of medium along the flow direction. In flow through porous media, intricate pore geometry creates a complex and spatially fluctuating velocity field and it is well-known that such flow variations at pore-level affect the transport processes in porous media and give rise to many anomalous behaviors which macroscopic models fail to predict, such as early breakthrough of the solute [6] or mixing-controlled reactions in heterogeneous media [7]. Naturally, it is of great interest to relate such complex velocity fields and resulting macroscopic transport properties to pore geometry.

Recent advances in porous media imaging techniques such as x-ray microtomography and pore-scale simulations have allowed for resolving the flow at the pore-scale for complex and realistic pore geometries. Computationally, fluid flow at pore-scale is investigated either through direct pore-scale or pore-network models. In the latter approach, the pore structure is approximated by a network of pores connected by throats. As a result, pore-network models do not preserve the original pore-space features. A review of pore-scale analysis using pore-network models is given in Ref. [8]. Direct pore-scale modeling, however, is achieved by solving governing equations directly on the pore-structure [9]. Recently, a direct comparison of velocity fields obtained by particle image velocimetry (PIV) and magnetic resonance imaging (MRI) with pore-scale simulations suggests that given an accurate representation of the pore geometry, DNS could predict accurately flow and transport at the pore-scale [10].

Pore-scale modeling has been intensively used to study the effects of pore geometry on transport properties such as hydraulic permeability [11–14], heat transfer [15], and solute dispersion [16,17]. For example, studies of Daneyko *et al.* [18] and Vidal *et al.* [19] suggest negligible effects of grain size distribution on the hydraulic permeability, whereas Garcia *et al.* [20] showed that the grain shape is a key parameter and could change permeability by a factor of 2. In a similar study, Pan *et al.* [21] proposed improvements to the existing empirical permeability relationships for sphere packing with various porosities and polydispersities. Contributions of flow inertia to permeability in regular and random sphere arrangements were evaluated in Ref. [22]. It was shown that the pore structure plays an important role on the drag force acting on the sphere packing along with the solid volume fraction and the direction of the flow. Anisotropy of the porous medium and its effects on the permeability were studied by Stewart *et al.* [23]. A correlation between the mean tortuosity and the porosity was proposed in stochastically generated porous media in Ref. [24].

Many recent observations have shown that displacement of solute could not be accurately predicted by advection-dispersion equation (ADE) [25] and this discrepancy is

 

often attributed to the extreme heterogeneity of the medium and significant changes in the local velocity field [26]. The signature of anomalous transport is the power-law tail of solute concentration long after its breakthrough [27]. Different stochastic models have been developed to address this anomalous behavior such as mobile-immobile concept [28], multiple-rate transfer models [29], fractional ADE [30], and continuous time random walk (CRTW) [31,32]. In the CTRW framework, the transport of solute is greatly affected by the behavior of transit time distribution, $\psi(t)$, where it is generally assumed that $\psi(t) \sim t^{-1-\beta}$. For example, truncated power-law (TLP) distribution for $\psi(t)$ has been particularly successful at describing anomalous transport [33]. However, the key parameter $\beta$ in $\psi(t)$, also a measure of medium heterogeneity, still needs to be determined. In fact, effective parametrization of such models requires knowledge of Eulerian and Lagrangian statistics of flow through porous media. For example, given the physical interpretation of $\psi(t)$, it can be determined from pore-scale velocity field [34,35]. Bijeljic and Blunt [36] used pore-network model of a Berea sandstone to determine transient time distribution where they observed a power-law distribution of pore-to-pore travel times.

Importance of detailed knowledge about underlying velocity distributions and correlations in porous media due to their impact on transport behavior and hydraulic properties of the media has led to intensive research focused on measuring velocity probability density functions (PDF) and its correlations through experimental and numerical techniques [37–39]. A combination of log-normal and exponential functions has been suggested [40] to describe the velocity distribution of slow flow in monodisperse bead packing for the low- and high-velocity regions of the velocity distribution, respectively. Velocity distribution for low and moderate Reynolds number flows were reported by Icardi *et al.* [41] in porous media generated by irregular nonconvex polydisperse objects. They obtained almost symmetric distribution for transverse components of velocity with increasing variance with respect to Reynolds number. It was pointed out that the streamwise velocity distribution is highly skewed for low Darcy velocities showing an intensified negative tail as Darcy velocity increases, indicating the existence of recirculation zones. Recently, it was shown that for two-dimensional models of fibrous material, PDFs of all velocity components follow a power-law with some tuning parameters [42]. In an experimental study by Patil and Liburdy [43], they observed in planes near the bed walls where flow is nearly two-dimensional, pore-space and velocity autocorrelations feature the same patterns but such patterns vanish in central planes. Using confocal microscopy and PIV, Datta *et al.* [44] showed that in a channel comprised of glass beads, 2D velocity components follow an exponential behavior. Moreover, they presented strong relationship between spatial fluctuations of 2D velocity field with pore-space geometry.

In this work, we study Eulerian and Lagrangian velocity PDFs by means of high resolution direct numerical simulation of Navier-Stokes equations at the pore-scale. Our emphasis is on characterizing statistics of flow and transport and their relationships to pore-space. We study how Eulerian velocity PDFs vary with respect to medium properties (i.e., porosity) and their correlations for two distinct models of porous media namely nonoverlapping hard-sphere and overlapping sphere models of porous media. Later on, we study Lagrangian velocity PDFs sampled isochronally and equidistantly along the particle trajectory and their evolutions with time and space. We investigate the Lagrangian velocity PDFs and their relationship with their Eulerian counterpart. Transport properties of porous media are obtained using a streamline approach through analyzing first-passage time distributions and mean tortuosity. We show that wider Eulerian velocity PDFs and higher tortuosity for overlapping sphere system yield in more anomalous transport compared to hard-sphere system where Eulerian velocity PDFs and tortuosity show narrower distributions and smaller values, respectively. Finally, we analyze the correlation functions of pore-space and Eulerian velocity field and show that not only for rather homogeneous porous media composed of spheres in 3D, but also for natural rocks there exists a strong relationship between these correlation functions.

## II. NUMERICAL METHOD

The fluid flow is described by the mass and momentum conservation equations:

$$\nabla \cdot \mathbf{u} = 0, \tag{2}$$

$$\frac{\partial(\rho \mathbf{u})}{\partial t} + \nabla \cdot (\rho \mathbf{u}\mathbf{u}) = -\nabla p + \nabla \cdot (\rho \nu \nabla \mathbf{u}). \tag{3}$$

Conservation equations are solved using a finite volume method (FVM) and a projection method [45] by using the parallel robust interface simulator (PARIS) [47]. Equation (3) is discretized on a staggered grid configuration where no-slip and no-penetration boundary conditions are enforced on the fluid-solid interface. Convection and diffusion terms in Eq. (3) are discretized using QUICK and central difference schemes [46], respectively, and time integration is performed using an Euler explicit scheme. The resulting Poisson equation is solved by Biconjugate gradient stabilized method (BiCGSTAB) with the residual tolerance of $10^{-8}$. The computational domain is a cube where a periodic boundary condition is prescribed on all boundaries. A constant pressure gradient (i.e., body force per unit mass) is applied to induce the flow from left to right in the $x$ direction. In many applications of flow through porous media such as enhanced oil recovery, given the physical properties of water, typical flow rate of 1 ft/day ($u$) and average pore size of 10 $\mu$m ($l$) results in Re $\ll 1$ where $\mathrm{Re} = \frac{\rho u l}{\mu}$. In this paper, we study flow and transport through porous media in the creeping flow regime (Re $\ll 1$). The results are reported after a steady-state condition is achieved based on the criterion given by Botella and Peyret [48].

### A. Validation

In this section we show the validation of our simulations. For the purpose of validation, we compare our results with experimental data by Suekane *et al.* [49] and numerical results of the same experiment by Finn and Apte [50]. In the experiment, pore-scale velocity measurements were carried out for flow packed bed using magnetic resonance imaging (MRI). Figure 1 shows a comparison for the normalized velocity. There is an excellent agreement between predicted velocity profile

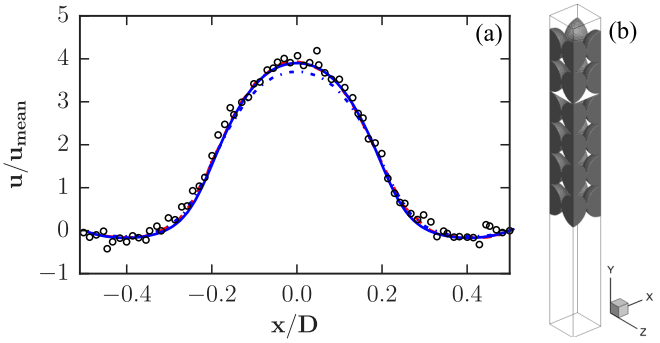


FIG. 1. (a) Comparison of interstitial velocity profiles at Re = 105.57 with experimental data of Suekane *et al.* [49] (◯) and numerical results of the same experiment by Finn and Apte [50] (−−). − simulation data with grid spacing of $\Delta/\mathrm{D} = 56$; · − · simulation data with grid spacing of $\Delta/\mathrm{D} = 28$. (b) Schematic of the experimental setup of Suekane *et al.* Simulation is performed with four lateral faces as wall and inflow and outflow boundary conditions for bottom and top faces, respectively, according to the experiment of Suekane *et al.* Normalized velocity is measured along the centerline of the plane shown in white (along $x$ axis). Solids are colored gray.

and experimental data. Moreover, Fig. 1 shows the effect of grid resolution on the predicted velocity profile. Additionally, we obtained $k/D^2 = 6.82 \times 10^{-4}$ for the permeability of monosized sphere pack for $\phi = 35.8\%$, which is close to $k/D^2 = 6.8 \times 10^{-4}$ reported by Bryant and Blunt [51] for the same system and for $\phi = 36.2\%$.

### B. Porous media

In this work, we build porous media via arranging spheres in a 3D space. A wide range of real heterogeneous porous media can be represented by considering two distinct categories of packing, (a) impenetrable (hard-) sphere model and (b) fully penetrable (overlapping) sphere model [52]. In the latter model, also known as boolean model, spheres centers are points of a stationary Poisson process. Boolean model is an extreme case of a penetrable-concentric-shell (cherry-pit) model where impenetrability parameter is zero. In the case of hard-sphere model, the impenetrability constraint makes it difficult to analyze and generate such systems specially at high solid volume fractions [53]. There are a number of techniques for generating (jammed) packing of hard-spheres. In this work, we adopted the collision-driven molecular dynamics algorithm of Ref. [54], which is essentially a generalization of Lubachevski-Stillinger (LS) algorithm [55]. In LS algorithm, spheres are initially added sequentially in a periodic box at a small volume fraction. Spheres then evolve in time while their radii grow at rates proportional to their radii until the desired packing is achieved. Polydispersivity gives more flexibility in representing a wide class of microstructures. Thus, we further generalized this algorithm based on the work of Ref. [56] to generate dense polydisperse sphere packings. In the case of polydisperse spheres with $M$ classes of spheres, density function of sphere radii is given by

$$f(r) = \sum_{j=1}^{M} y_i \delta(r - r_i), \tag{4}$$

where $y_i = \frac{N_i}{N}$ and harmonic mean particle diameter $\overline{D}$ is defined as

$$\overline{D} = \frac{\sum_{j=1}^{M} N_i D_i^3}{\sum_{j=1}^{M} N_i D_i^2}, \tag{5}$$

which is used to normalize all lengths in the problem. Since particle size distribution of many granular systems is found to be approximately log-normal [57], spheres radii probability density function takes the form

$$f(r) = \frac{1}{r\sigma\sqrt{2\pi}} \exp\left[-\frac{(\ln(r) - \mu)^2}{2\sigma^2}\right], \tag{6}$$

where $\sigma$ and $\mu$ are variance and average of $\ln(r)$, respectively. In LS algorithm, the initial configuration, expansion rate, and initial distribution of particle velocities affect the final packing. It is also worth noting that the expansion rate must be chosen carefully as small values lead to local crystallization while a relatively large ones will not produce random close packing. Finally, we build the overlapping sphere model by placing monosized spheres in random locations within the computational domain sequentially until the desired porosity is achieved. In this study, we use three models of porous media including monodisperse hard-spheres, polydisperse hard-spheres, and overlapping spheres with different porosities by changing the number of spheres in the system where all the porous media have the same harmonic mean particle diameter ($\overline{\mathrm{D}}$) (Fig. 2).

### C. Characterization of porous medium

Characterization of the microstructure of porous media plays an important role in determining macroscopic properties such as residual saturation of nonwetting phase, permeability, reaction constant, etc. Microstructure of porous media can be characterized by $n$-point probability functions [58], Voronoi statistics [59], fractal geometry [60,61], local-porosity theory [62], Minkowski functional [63], and pore size distribution [64], to name a few. Our aim here is to connect our findings about flow in porous media to such statistical descriptors. Each realization of the porous medium is a domain of space $\mathcal{V} \subseteq \mathbb{R}^3$ consisting of two disjoint phases namely pore and grain. Thus, each phase could be identified through an indicator function $\mathcal{I}^i(r)$ for phase $i$ as

$$\mathcal{I}^i(r) = \begin{cases} 1 & r \in \mathcal{V}_i \\ 0 & \text{otherwise.} \end{cases} \tag{7}$$

Complete statistical description of a medium is then obtained by means of $n$-point correlation function $S_n^i$ given as

$$S_n^i(r_1, r_2, \ldots, r_n) = \left\langle \prod_{j=1}^{n} \mathcal{I}^i(r_j) \right\rangle, \tag{8}$$

where $\langle \cdots \rangle$ denotes the ensemble average over all the possible positions $r$ and $S_n^i$ defines the probability of finding $r_1, r_2, \ldots, r_n$ all in the phase $i$. For statistically isotropic material (i.e., joint probability distributions are invariant of coordinates rotation) $n$-point correlation function depends only on the relative position of points rather than their absolute positions [65]. Hereafter, for simplicity, we drop the superscript

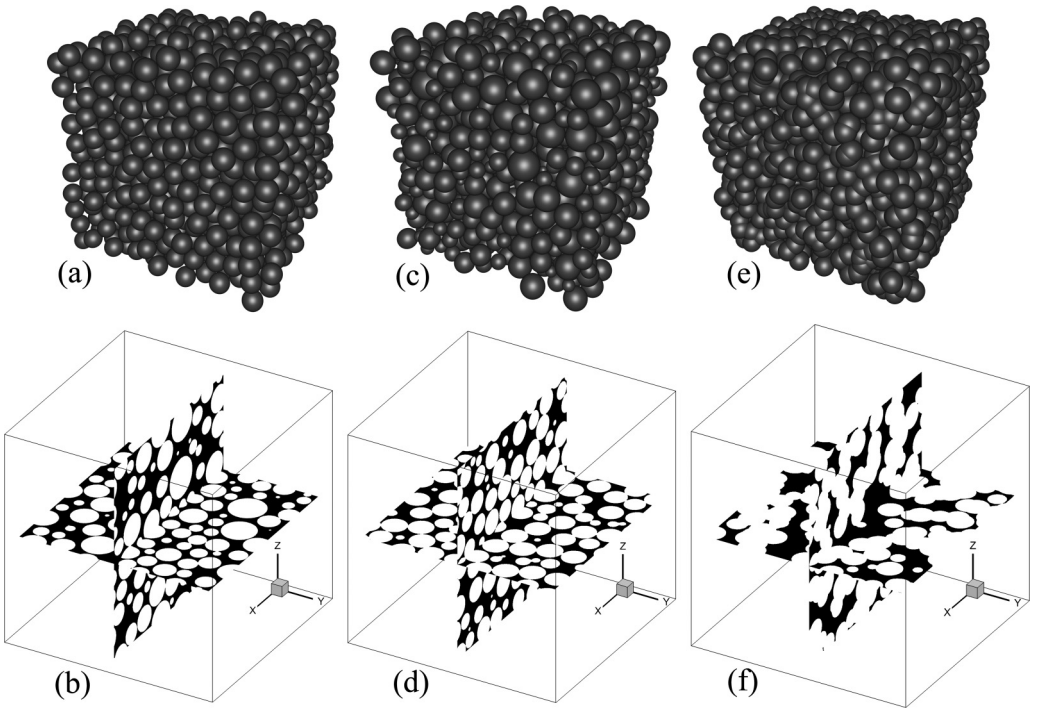


FIG. 2. Three-dimensional periodic assemblies of spheres and cross sectional views of indicator function (solid or pore-space) for (a), (b) monodisperse hard-spheres, (c), (d) polydisperse hard-spheres, and (e), (f) (monodisperse) overlapping spheres. Pore-space is colored black.

$i$ and let $\mathcal{I}$ to be indicator function of the pore phase. Perhaps the simplest and most important characteristics of a porous medium is its porosity (i.e., the ratio of pore volume to total volume) and is given by the one-point correlation function as

$$S_1(r) = \langle \mathcal{I}(r) \rangle = \phi. \tag{9}$$

Among various statistical descriptors of random media, in this study we focus on two-point correlation functions as they arise in analytical estimations of many physical properties of random media and reveal their global structures [58]. These functions have been extensively used to characterize the porous media [66,67]. They could be used to estimate upper and lower bounds for fluid permeability, electrical conductivity, and magnetic fields [68]. Recently, Jiao *et al.* [69] used two-point correlation functions to model heterogeneous two-phase media. However, it is worth noting that two-point correlation functions cannot be sufficient alone to completely determine a medium [70] (i.e., for capturing long-range connectivity higher order statistics are required).

For two-phase medium two-point correlation functions have limiting behavior as [65,67]

$$\lim_{r \to 0} S_2(r) = \phi, \tag{10}$$

$$\lim_{r \to \infty} S_2(r) = \phi^2. \tag{11}$$

For isotropic two-phase medium, Debye *et al.* [71] showed that derivative of $S_2(r)$ at origin ($r = 0$) is in direct relationship with the specific surface area (s) of the medium as

$$\lim_{r \to 0} S_2^{'}(r) = -s/4. \tag{12}$$

This relationship was later generalized for anisotropic media by Berryman [72].

Blair *et al.* [66] showed that two-point correlation functions could also be used to obtain estimations of effective pore size and mean grain diameter. Additionally, the shape of two-point correlation functions reflects an underlying medium morphology. Thus, $S_2(r)$ plays an important role in this work as we later show that structure of $S_2(r)$ can determine that of velocity fluctuations in porous media regardless of how the porous media is constructed. Shown in Fig. 3 is $S_2$ for our three models of porous media.

### D. Determining representative elementary volume (REV)

Modeling of fluid flow at pore-scale or imaging porous media is limited to small samples. Thus, it is important to show that such data sets is representative of larger scale systems. The prerequisite for any analysis of porous medium for calculating macroscopic properties is evaluating the representative elementary volume of such medium. The concept of REV has different definitions in the literature [73]; however, it could be regarded as a length-scale at which flow obeys Darcy's law and macroscopic properties such as porosity and permeability are defined using volume averaging. Many different procedures exist for determining REV [73]. In this work we determine "statistical" REV with slight modifications in the procedure proposed in Ref. [74]. It is worth mentioning that in the statistical approach a sample is called REV if the mean and variance of the quantities of interest (e.g., porosity, specific surface) falls below a certain value [21]. Here, instead of generating a reference domain and then dividing it to smaller subdomains for further analysis, we increase the domain size incrementally and generate 20 independent packings for

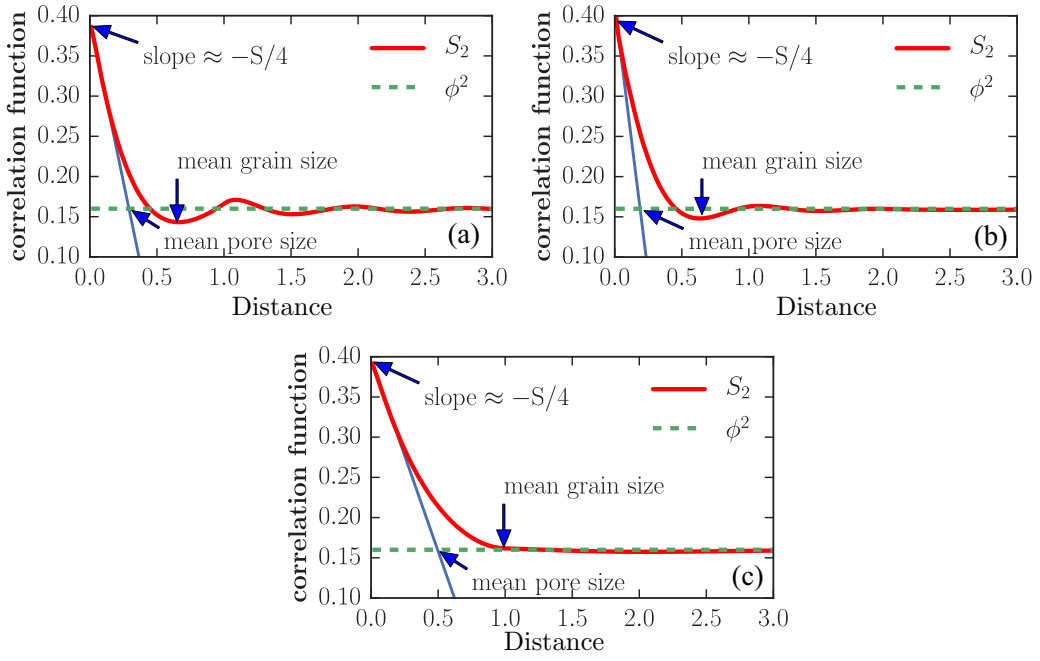


FIG. 3. Different models of porous media and their two-point correlation functions. Significant difference in the structure of $S_2(r)$ is an indication of different morphology of porous media models. In hard-sphere systems (a), oscillations in $S_2(r)$ is due to exclusion volume effect. These oscillations becomes weaker in the case of polydisperse hard-spheres (b), and completely vanishes for overlapping spheres (c). Different statistics could be obtained simply by calculating $S_2(r)$, as shown in the figure.

each increment in domain size. We believe this procedure provides a better way of doing such analysis as (i) every single medium satisfies periodicity in all directions which is consistent with boundary conditions used in numerical simulations, (ii) different packings generated for each domain size allows for variability in packing structure even when porosity is kept constant (i.e., we randomly choose the parameters affecting packing, see Sec. II B), (iii) this procedure eliminates boundary effects (e.g., wall) and the need for adding buffer layers to the outlet and inlet. We studied different REVs for porosity, specific surface area, and permeability and found that permeability gives the largest REV. Here, we define REV where coefficient of variation of permeability falls below 3%. Figure 4(a) shows that domain sizes with $L/\overline{D} \geqslant 5.0$, satisfies this criteria and thus are considered REV. Empirical variograms are useful in determining REV as they show the correlation of data with distance [75]. Thus, to further analyze and quantify how large our domain is with respect to spatial correlations and different length scales of the medium, we evaluated the empirical variograms of porosity and velocity in the direction of flow as

$$\gamma_p(h) = \frac{\sum_1^N [I(x_i + h) - I(x_i)]^2}{2N}, \tag{13}$$

$$\gamma_u(h) = \frac{\sum_1^N [u(x_i + h) - u(x_i)]^2}{2N}, \tag{14}$$

where $I$ is the indicator function for porosity [$I(x_i) = 1$ for pore-space and $I(x_i) = 0$ for solid space], and $N$ is the total number of points with the distance $h$. Figure 4(b) suggests that beyond one particle diameter ($\overline{D} \geqslant 1$), variograms of porosity and velocity become uncorrelated and hence our porous medium represents larger samples [76]. Table I summarizes values of two different characteristic length scales, namely, mean pore diameter ($l_c$) and integral length scale ($\lambda$), and ratios of domain size to these length scales. Mean pore diameters are calculated based on two-point correlations functions (see Fig. 3) as $\frac{\phi(1-\phi)}{S_2'(0)}$ [i.e., intersection of $S_2 = \phi^2$ and a tangent to $S_2(r)$ at $r = 0$]. Integral length scale of the spatial structure of each medium is calculated as

$$\lambda = \int_0^\infty S_2(r) dr. \tag{15}$$

Finally, we used a simulation box of size $L/\overline{D} = 8$ discretized into $480^3$ finite volumes to both eliminate finite-size effects and achieve grid independent results.

## III. LAGRANGIAN STATISTICS

In this section we study Lagrangian-based statistics of flow through porous media. Lagrangian description of flow field is obtained by means of particle tracking in the steady-state Eulerian flow field. In each simulation, $10^5$ tracer particles are introduced on the inlet face uniformly. Particle trajectory is then obtained via integration of Eq. (16) as

$$\frac{d\mathbf{x}(t)}{dt} = \mathbf{v}(\mathbf{x}(t)), \quad \mathbf{x}(t_0) = \mathbf{x}_0, \tag{16}$$

where a third-order Runge-Kutta scheme is used for time integration and a trilinear interpolation scheme is used to locally interpolate particle velocity from the fully resolved Eulerian field. We also performed computations where we used $10^4$ and $5 \times 10^4$ particles and confirmed that $10^5$ particles gives converged statistics. Particle tracking enables us to study useful

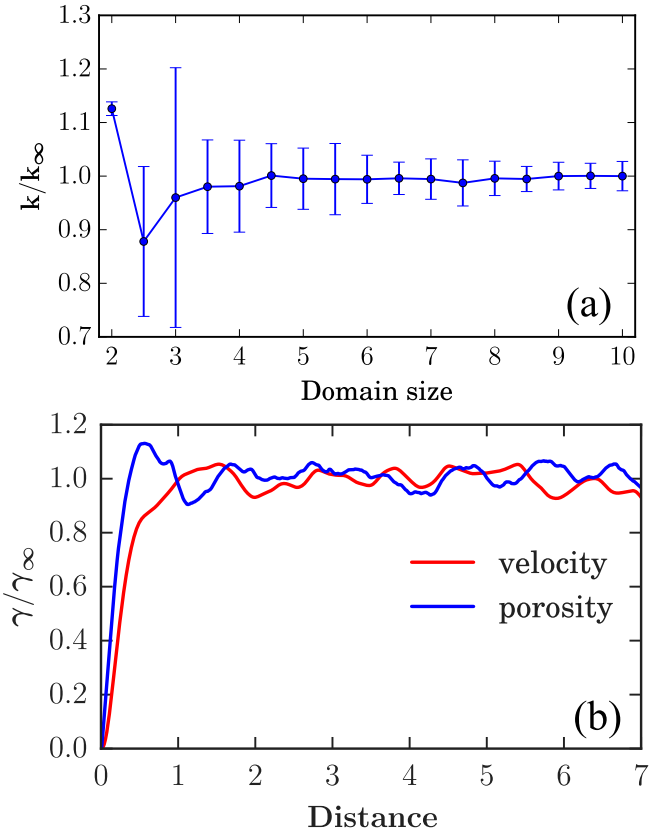


FIG. 4. Representative elementary volume calculation: (a) variation of permeability with respect to domain size; (b) variogram of porosity and velocity in the direction of flow normalized by their theoretical asymptotic values $\gamma_\infty = \phi(1-\phi)$ for porosity and $\gamma_\infty = \langle u^2\rangle - \langle u\rangle^2$ for velocity variograms. Variograms are plotted as functions of distance from the inlet face. Data is for the monodisperse hard-sphere model at $\phi = 0.40$.

quantities such as trajectory length, breakthrough curves, and tortuosity. Figure 5 shows variations of trajectory length distribution for three models of porous media. For all three types of porous media, trajectory length distributions are highly conditioned by porosity. Interestingly, trajectory length distributions for the hard-sphere model exhibit less skewness compared to those of overlapping spheres at the same porosity where long-tailed particle trajectory length distribution is observed. Such long tails signify highly tortuous pathways due to closing off of pore throats as spheres overlaps in the overlapping spheres model whereas in porous media composed of hard-spheres pore-space is hydrodynamically well connected. Overall, it is clear that trajectory length distributions are different for each case such that as we move from overlapping sphere to hard-sphere model and from low to high porosities, the mean trajectory length as well as its variation reduces (Table II). From the data in Fig. 5, we can calculate the tortuosity for different models of porous media. Elongation of streamlines in flow through porous media, captured by tortuosity, impacts medium's permeability and its transport properties and thus has been studied intensively in the literature [77–84]. In this work tortuosity is defined as

$$T = \frac{\langle \lambda \rangle}{L}, \tag{17}$$

where $\langle \lambda \rangle$ is the average trajectory length traveled by all the particles while no flux weighting is involved and $L$ represents the straight line connecting injecting and absorbing sites (i.e., inlet and outlet boundaries here). Generally, obtaining fluid trajectories to be used in Eq. (17) is notoriously difficult both experimentally and numerically in complex geometries. Alternatively, it has been shown that tortuosity could be obtained by calculating $\frac{\langle \boldsymbol{u} \rangle}{\langle u_x \rangle}$ [81]. This simple equation, however, has limitations due to existence of recirculation zones in flow through porous media as mentioned by Duda *et al.* [79]. Here we extended the work of Matyka *et al.* [82] by directly calculating tortuosity in our two distinct classes of porous media. Figure 6 shows the variation of tortuosity calculated using Eq. (17) for porous media comprised of hard-spheres and overlapping spheres. We found that tortuosity scales well with porosity for the range of porosity $0.36 < \phi < 0.60$ according to two empirical relations [78,85] as

$$T = 1 - p \ln(\phi), \tag{18}$$

$$T = 1 - p(1-\phi), \tag{19}$$

where $p$ is a constant parameter equal to 0.26 and 0.55 for hard-sphere and overlapping sphere models, respectively. The values reported here for hard-sphere systems is in excellent agreement with tortuosities reported by Muljadi *et al.* [86] for the same medium using the indirect formula of Koponen *et al.* [81] as well as geometric tortuosity values reported by Sobieski *et al.* [84]. Here streamlines are uniformly initiated at the inlet plane; we expect tortuosity values to be even smaller when streamlines are initiated in a flux-weighted fashion. It was also found that polydispersivity has negligible effect on tortuosity. Tortuosity is linked to transport phenomena in porous media and its macroscopic properties such as dependence of permeability in Kozeny-Carman theory on tortuosity [41,79,87]. It is thus expected that different values of tortuosities result in differences in transport properties. To investigate the effect of our two distinct pore-structures on the nature of transport, we have studied the transport of solute particles using streamline approach in purely advective flows (in the absence of diffusion).

Here, we calculated the first-passage time of solute particles, which is the travel time required for a particle to percolate through the porous medium. First-passage time distribution (FPTD), in fact, could be seen as $\psi(s,t)$ with displacement equal to the distance between injecting and absorbing sites. We associate $\psi(t)$ to FPTD and directly calculate the key parameter $\beta$ from pore-scale simulations for two models of porous media. It is worth noting that although the models of

TABLE I. Mean pore size ($l_c$) and integral length scale ($\lambda$) of nonoverlapping and overlapping systems.

| Porous medium | $\phi$ | $l_c$ | $\lambda$ | $L/l_c$ | $L/\lambda$ |
|---|---|---|---|---|---|
| Monodisperse hard-spheres | 0.45 | 0.29 | 0.14 | 27.58 | 57.14 |
| Polydisperse hard-spheres | 0.45 | 0.17 | 0.15 | 47.00 | 53.33 |
| Overlapping spheres | 0.45 | 0.50 | 0.30 | 16.00 | 26.66 |

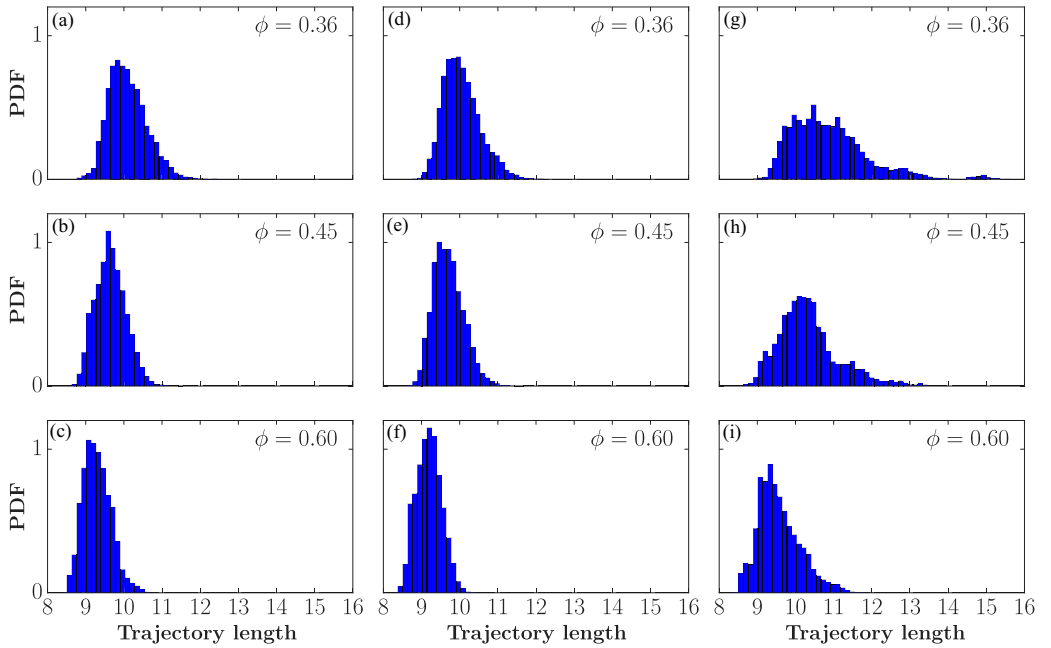


FIG. 5. Variation of trajectory length distribution with respect to porosity for (a)–(c) monodisperse hard-sphere, (d)–(f) polydisperse hard-sphere, and (g)–(i) overlapping sphere models of porous media.

porous media examined here are idealized ones, but they, in fact, represent two opposite extremes of porous media classes. For example, overlapping spheres at low porosities can be used as models for consolidated media such as sandstone, while hard-sphere model could represent unconsolidated media such as packed beds and particulate composites [65]. Using pore-scale simulations on two different types of porous media, we obtained parameter $\beta$ which could be seen as degree of medium heterogeneity [36]. Shown in Fig. 7 is FPTD for two models of porous media and two porosities. Transport of solute plume in the hard-sphere model is Fickian (i.e., $\beta > 2$). However, overlapping sphere medium shows anomalous behavior (i.e., $\beta < 2$) with parameter $\beta = 1.8$. This is interestingly close to the value reported by Bijeljic and Blunt [36], which was obtained for two-dimensional model of Berea sandstone, corroborating the fact that the model of overlapping spheres could be used to represent consolidated systems. Moreover, the shape of FPTD is consistent with trajectory length distributions where there exists a long tail of particle trajectories for the case of overlapping spheres while in the case of hard-sphere model, trajectory length distributions are essentially symmetric and do not exhibit long-tailed behavior.

Now, we study the Lagrangian velocity statistics and their evolution. Lagrangian description of particle velocity consists of two viewpoints which is analyzing Lagrangian velocities sampled isochronally and equidistantly along streamlines. Studies on flow through porous media and observations of intermittency of fluid velocities suggest that particle velocities persist for a characteristic length scale $l_c$ rather than a characteristic timescale $\tau_c$ [35]. Thus, stochastic description of particle transport in porous media is based on the distribution of Lagrangian velocities sampled equidistantly along streamlines. Naturally, it is important to quantify the velocity statistics in these two frameworks and their relations to the Eulerian

TABLE II. Mean, standard deviation (SD), minimum, maximum, and skewness of trajectory lengths for different monodisperse models of porous media and porosities.

| Porous medium | $\phi$ | Mean | SD | Min | Max | Skewness |
|---|---|---|---|---|---|---|
| Hard-sphere | 0.36 | 10.09 | 0.49 | 8.74 | 12.60 | 0.57 |
| | 0.45 | 9.65 | 0.39 | 8.57 | 11.45 | 0.27 |
| | 0.60 | 9.29 | 0.36 | 8.47 | 10.71 | 0.45 |
| Overlapping | 0.36 | 10.86 | 1.01 | 8.97 | 16.08 | 1.23 |
| | 0.45 | 10.33 | 0.79 | 8.69 | 13.69 | 0.91 |
| | 0.60 | 9.57 | 0.55 | 8.50 | 12.18 | 0.75 |

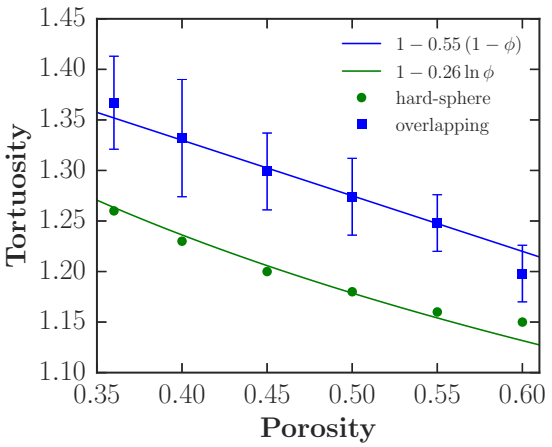


FIG. 6. Variation of tortuosity with different models of porous media and porosity. Error bars for the case of hard-sphere model are the size of symbols and thus not plotted.

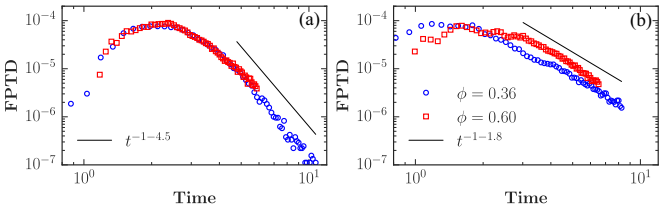


FIG. 7. First-passage time distribution for (a) monodisperse hard-spheres and (b) overlapping spheres for high (□) and low (◯) porosity media.

velocity field. Recently, Dentz *et al.* [34] provided expressions that relate Lagrangian velocity statistics to those of Eulerian. Here, we briefly review these relations and proceed to our analysis of Lagrangian statistics. We first consider particle velocity along its trajectory as a function of travel distance, $s$. According to Dentz *et al.* [34], the PDF of $s$(pace)-Lagrangian and $t$(ime)-Lagrangian velocities are related through flux-weighting as

$$p_s(v) = \frac{v p_t(v)}{\langle v_t \rangle}, \tag{20}$$

where $\langle v_t \rangle = \int v p_t(v) dv$. Furthermore, due to volume conservation, $t$-Lagrangian velocity PDF, $p_t(v)$, is equal to Eulerian velocity PDF, $p_e(v)$. Thus, this means that $p_s(v)$ is related to $p_e(v)$ through flux weighting as

$$p_s(v) = \frac{v p_e(v)}{\langle v_e \rangle}, \tag{21}$$

where $\langle v_e \rangle = \int v p_e(v) dv$. It is worth noting that Eq. (21) is valid under stationary condition. $T$- and $s$-Lagrangian velocity distributions evolve in time and space if their initial distribution is different than their steady-state one. Clearly, at $t = 0$ and $s = 0$ both $p_s(v)$ and $p_t(v)$ are identical and equal to initial particle velocity distribution, $p_0(v)$. Furthermore, under Eulerian ergodicity and uniform injection, which is the case here, $t$-Lagrangian velocity PDF coincides with Eulerian velocity PDF and thus does not evolve [34,88]. However, $s$-Lagrangian velocity distribution for the case of uniform injection evolves toward its steady-state PDF given in Eq. (21). Figure 8 shows the evolution of mean $s$-Lagrangian velocity. As expected, at $s = 0$ the mean $s$-Lagrangian velocity (and mean $t$-Lagrangian velocity) is equal to the mean Eulerian velocity. However, mean $s$-Lagrangian velocity evolves to its steady-state value, while mean $t$-Lagrangian velocity remains constant and equal to mean Eulerian velocity. It is worth noting that mean $s$-Lagrangian velocity converges faster to its steady-state value for the case of monodisperse hard-sphere model compared to overlapping sphere model due to relatively simpler pore-structure. Finally, using Eq. (21), we can calculate the stationary $s$-Lagrangian velocity distribution and compare it with the distribution obtained from numerical simulation and particle tracking. Figure 9 shows that measured $s$-Lagrangian velocity PDF agrees well with the flux weighted Eulerian velocity PDF.

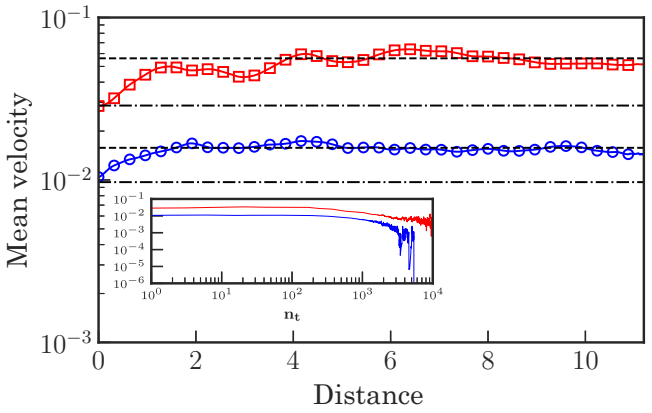


FIG. 8. Evolution of the mean velocity sampled equidistantly in space for hard-sphere (◯) and overlapping sphere (□) models. Due to uniform injection of particles, mean velocity sampled equidistantly in space evolves from its initial value which coincides with mean Eulerian velocity ($\cdot - \cdot$) and reaches its steady-state value calculated from Eq. (21) ($--$). Inset: Mean velocity sampled isochronally remains constant until breakthrough and is equal to mean Eulerian velocity as expected. $n_t$ is the number of time steps.

## IV. EULERIAN STATISTICS

A complete picture of velocity field is extremely useful in understanding transport in porous media. For example, Tennekes and Lumley [89] showed that mechanical dispersion ($D_L$) is directly related to the Lagrangian velocity of a particle ($V_L$) and Lagrangian integral timescale ($T_L$) as

$$D_L \cong \overline{(V_L - \overline{V_L})^2} T_L. \tag{22}$$

Patil and Liburdy [43] replaced the Lagrangian velocity variance with Eulerian velocity variance under the assumption of $V_L$ being stationary and estimated the mechanical component of longitudinal dispersion. Although it has been shown that difference in pore-space structures has significant effects on the velocity distribution at the pore-scale as well as changing the nature of transport, a quantitative study showing the interplay of pore structure, velocity, and transport is still lacking. One can imagine that due to incompressibility of fluid, local velocity

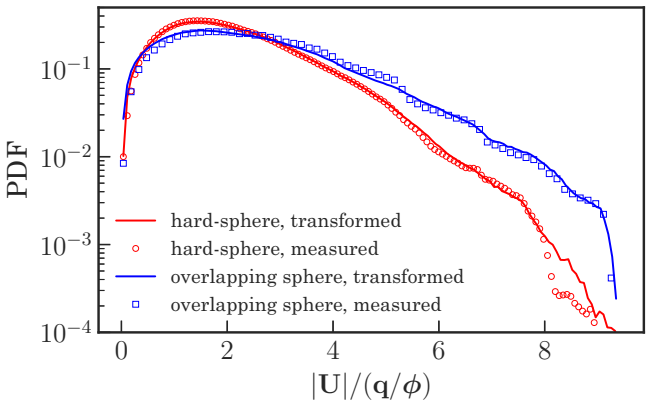


FIG. 9. Comparison of stationary $s$-Lagrangian velocity PDF as given by Eq. (21) and numerical simulation.

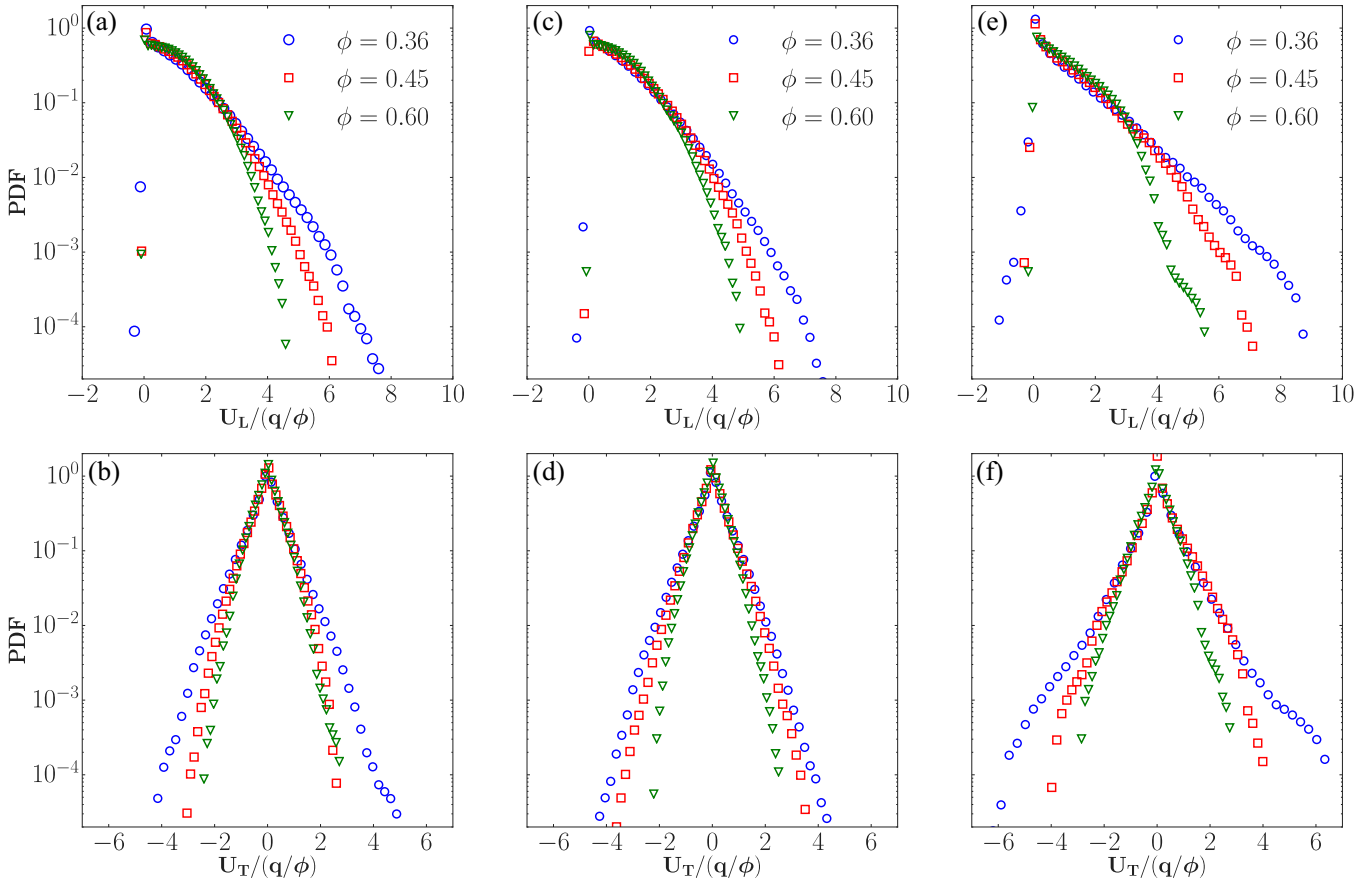


FIG. 10. Top row: PDF of streamwise velocity. Bottom row: PDF of velocity perpendicular to mean flow direction (spanwise). All velocities are normalized by mean interstitial velocity $(q/\phi)$ for (a), (b) monodisperse hard-sphere, (c), (d) polydisperse hard-sphere, and (e), (f) overlapping sphere models of porous media.

changes as fluid go through network of throats and pores of different sizes. This simple argument suggests that given the pore and throat size distribution of a medium, the velocity distribution must obey the same distribution, a fact that was studied by Siena *et al.* [39] where they found that the pore size and velocity distributions decay similarly. However, such a relationship is not always very simple as spatial correlation of pore and throat sizes has also found to be an effective parameter [39].

Here, we first look at the velocity distribution for our three models of porous media with increasing level of pore-space complexity over a range of porosities. Then, we focus on generalizing such velocity PDFs. Figure 10 shows that the velocity is broadly distributed and despite the randomness of pore-space in different models of porous media, its distribution shows some universality. It is worth noting that in all the cases shown in Fig. 10, there exist the following common feature as (i) the peak in PDFs locates at zero and it becomes more significant as porosity reduces, (ii) all the PDFs have both negative and positive tails, the latter is due to the tortuous flow path. This effect is the strongest in the case of overlapping spheres, which is supposed to result in the most complex pore-space among the models examined here, (iii) in all the cases here, velocity distribution becomes less broad as porosity increases and the positive tail of velocity distribution decays faster, (iv) spanwise velocity components are symmetric with a peak value at zero, similar to the streamwise component of velocity. One can see by looking at Fig. 10 that flow in overlapping spheres model results in broader range of velocity compared to hard-sphere models. Additionally, Fig. 11 shows the velocity norm distributions of monodisperse hard-sphere and overlapping sphere models in log-log scale. It reveals a significant difference in velocity norm PDF of these two models in low velocity

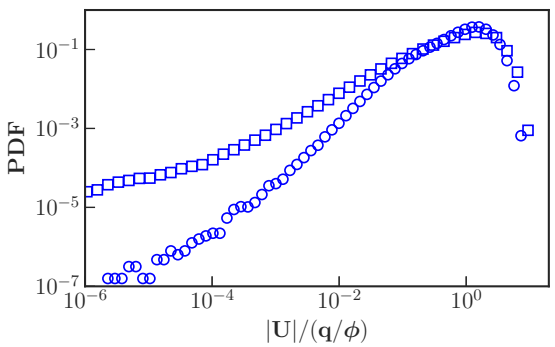


FIG. 11. PDFs of velocity norm for monodisperse hard-sphere (◯) and overlapping sphere (□) models for $\phi = 0.36$.

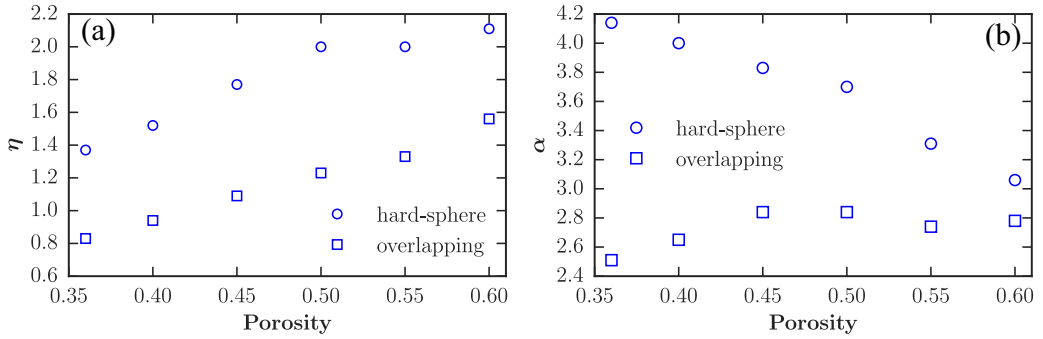


FIG. 12. Dependence of model parameters in Eq. (23) on porosity for two models of porous media (hard-sphere and overlapping). $\eta$ strongly depends on the porosity and is consistently larger for hard-spheres (a). However, the dependence of $\alpha$ on the porosity is not very strong (b). This figure clearly quantifies the transition in velocity distribution shape as a function of porosity.

ranges. As shown in Fig. 11, greater portion of pore-space in overlapping sphere model experiences very low velocities, which is consistent with the transport behavior shown in Fig. 7. Quantitatively speaking, streamwise velocity variance scales as $0.89\langle u\rangle^2$ compared to $1.21\langle u\rangle^2$ for hard-sphere and overlapping sphere models, respectively. Since there is no long-range correlation of pore-space in our models of porous media (see Fig. 3), we can explain this by studying pore-size distribution functions of these models. Klatt and Torquato [90] numerically estimated complementary cumulative distribution functions (1-CDF) of pore sizes ($F_\delta$) for monodisperse hard-spheres and overlapping spheres. Consistent with our velocity PDFs, they showed that $F_\delta$ decays much slower for overlapping spheres compared to hard-spheres, resulting in a broader pore size distribution and also larger effective pore-diameter (see Fig. 3). To generalize the velocity PDFs, we focus on the positive tail of distribution as the contribution of the negative tail to transport is negligible. The velocity distribution could be divided into two regions: first region ($u < \langle u\rangle$) is characterized by very small velocities due to existence of extensive fluid-solid interfaces and stagnant zones (see normalized velocities around zero in Fig. 10) and second region ($u > \langle u\rangle$) which is responsible for most of transport and is characterized by the structure of sample-spanning network of pores and throats [91]. Here, we adopted a stretched exponential distribution as [42]

$$f(u/\langle u\rangle) = a\exp\left[-\left(\frac{u/\langle u\rangle}{\alpha}\right)^{\eta}\right], \tag{23}$$

where parameter $\eta$ controls the shape of the positive tail (e.g., exponential or normal) and $\alpha$ indicates the decay rate. Parameter $a$ is a normalizing factor such that Eq. (23) is integrated to one and thus is given by $\frac{\eta}{\alpha\Gamma(1/\eta,1/\alpha^{\eta})}$ where $\Gamma$ is the incomplete gamma function. Figure 12 shows that $\eta$ heavily depends on the porosity and exhibits a transition from subexponential ($\eta < 1$) to normal ($\eta \approx 2$).

Velocity distributions for models of porous media in this study showed broad dynamic ranges of velocity which can be estimated by Eq. (23) accurately for several decades in probability (Fig. 13). Despite the usefulness of velocity distribution, they cannot be used to learn about spatial correlations of velocity field, while such correlations are critically informative as the flow pass through tortuous paths and channels of high and low velocities. Thus, to examine the spatial features of velocity, we calculated two-point correlation function of 3D velocity field which averages the scalar product of all velocity

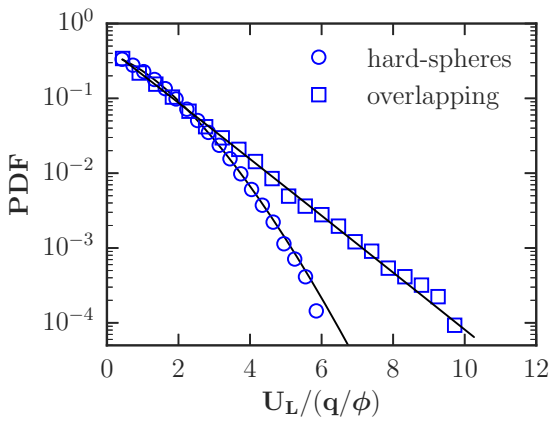


FIG. 13. Streamwise velocity distributions for (monodisperse) hard-sphere and overlapping sphere models of porous media with their corresponding fits obtained by Eq. (23) (solid line). Porosity is 0.45.

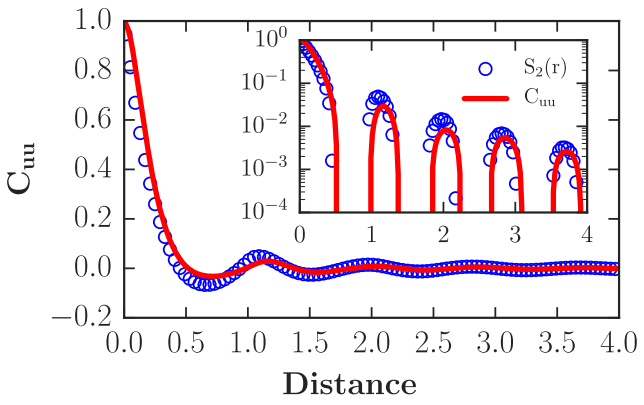


FIG. 14. Spatial correlation in velocity fluctuations for monodisperse hard-sphere model along with their two-point correlation function calculated on pore-space. Strong similarities suggests spatial correlations of velocity and pore-space are almost identical in the creeping flow regime.

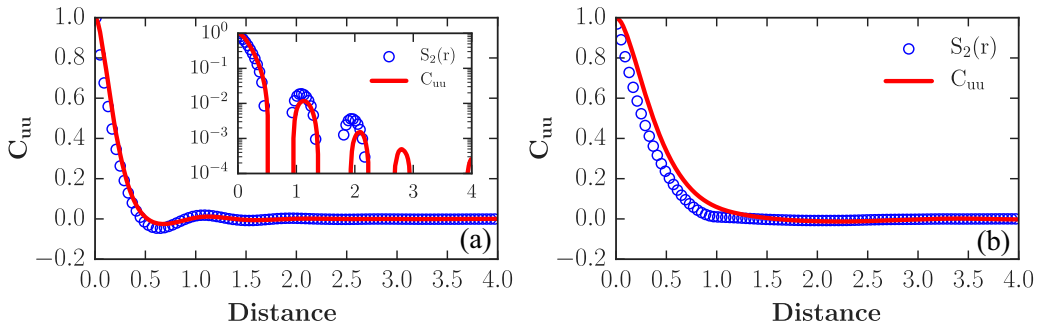


FIG. 15. Spatial correlation in velocity fluctuations for (a) polydisperse hard-sphere and (b) overlapping sphere models along with their two-point correlation function calculated on pore-space.

vector pairs separated by distance $R$ by

$$C_{uu}(R) = \left\langle \frac{\sum_j [u'(r_j)u'(r_j+R)]}{\sum_j \|u'(r_j)\|^2} \right\rangle, \tag{24}$$

where $u' = u - \overline{u}$ and the summation is taken over $10^4$ positions $r_j$ randomly chosen in the simulation domain. Figure 14 shows $C_{uu}$ and $S_2$ obtained for monodisperse hard-spheres. In particular, $C_{uu}$ is strongly similar to $S_2(r)$, shows a nearly exponential decay. We show that spatial features in velocity field are exactly the same as those of pore-space. The oscillations in $S_2(r)$ due to exclusion volume effects are reflected on pore-scale velocity fluctuations causing velocity fluctuations to be slightly correlated at large distances. To further generalize these findings, we carried out the same analysis on more complex pore geometries such as those in polydisperse hard-spheres and overlapping spheres.

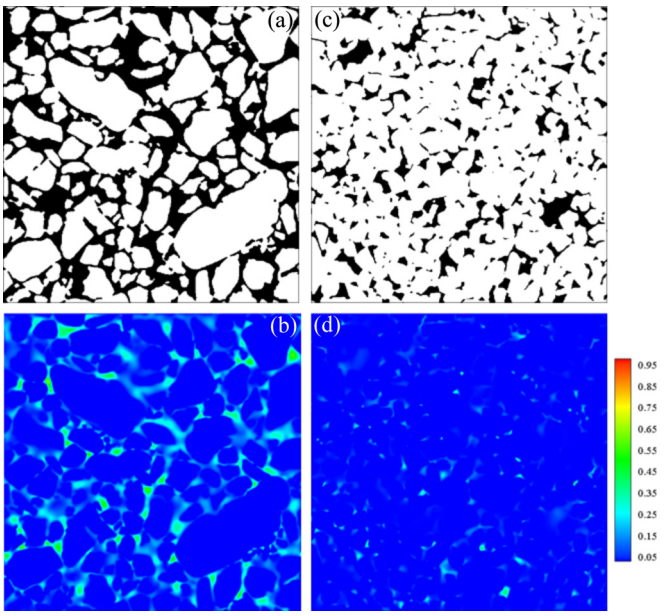


FIG. 16. Cross-sectional view of the indicator function (solid or pore-space) and normalized velocity magnitude ($|U|/|U|_{max}$) for (a), (b) the unconsolidated sandpack and (c), (d) Castlegate sandstone with porosity of 36% and 20.6%, respectively. Pore-space is colored black.

Interestingly, results shown in Fig. 15 suggest that even in completely different pore structures such as those in overlapping sphere model, spatial correlations of velocity are reflective of those of pore-space. Observed strong relationship between pore-structure characteristics and spatially fluctuating velocity field motivated us to see if such a relationship exists for natural rocks. We used cube samples ($512 \times 512 \times 512$) of unconsolidated sandpack and Castlegate sandstone with voxel size of 9.184 and 5.6 $\mu$m, respectively (data is publicly available at https://www.digitalrocksportal.org). These samples are originally obtained via x-ray micro-CT and then segmented where each voxel is identified as either void or solid. Porosity is 0.36 and 0.206 for unconsolidated sandpack and Castlegate sandstone, respectively. Figure 16 shows two-dimensional cross sections of the segmented image of these samples. To confirm that observed relationship between pore-space characteristics and fluctuating velocity field does not exist due to spatial homogeneity of the pore-space in hard-sphere and overlapping sphere models, similar analysis was performed on samples of unconsolidated sandpack and Castlegate sandstone. Figure 17 shows that consistent with what we observed previously for overlapping sphere and mono(poly)disperse hard-sphere models, a similar relationship exists in natural rocks as well where two-point correlation functions of pore-space and fluctuating velocity field decay similarly.

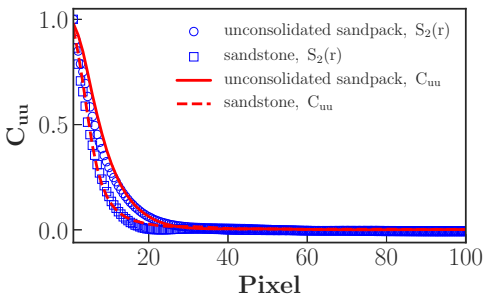


FIG. 17. Spatial correlation in velocity fluctuations for different models of porous media along with their two-point correlation function calculated on pore-space. Strong similarities suggest spatial correlations of velocity and pore-space are almost identical in the creeping flow regime.

## V. CONCLUSION

We investigated the flow through porous media through direct numerical simulation for three models of porous media with increasing levels of pore-space complexity. We showed that the Eulerian velocity field has a broad dynamic range which reflects the complexity of the pore-space. It was shown that streamwise Eulerian velocity distributions in virtually all porous media could be accurately modeled by a stretched exponential function which captures the transition from nearly exponential to Gaussian shapes of Eulerian velocity distribution for several decades in probability as porosity increases. A streamline particle tracking approach was used to calculate the Lagrangian statistics in an advection-dominant transport regime. We showed that particle trajectory in overlapping sphere model compared to hard-sphere model was more tortuous and its distribution had higher skewness. We then showed by means of FPTD that higher tortuosity and broader Eulerian velocity distributions of nonoverlapping sphere model resulted in non-Fickian transport (with quantitative agreement with transport in sandstone), while transport in the hard-sphere model was found to be Fickian. Evolution of Lagrangian velocity distributions, sampled isochronally and equidistantly along the particle trajectory were studied for the uniform injection rule and it was found that mean $s$-Lagrangian velocity evolves in space and reaches stationary condition quickly (takes longer for overlapping sphere model compared to hard-sphere model due to more complex pore-structure) while mean $t$-Lagrangian velocity does not evolve in time. Under stationary condition, $s$-Lagrangian velocity distribution is related to Eulerian velocity distribution through flux-weighting. Finally, we studied the spatial correlations in 3D velocity field by means of two-point correlation functions of velocity fluctuations. For the relatively homogeneous porous media examined here (overlapping and nonoverlapping spheres in 3D), we showed that the two-point correlation function of 3D velocity field decays similarly to that of pore-space and even at long distances displays similar oscillations. We tested the generality of this finding on two more heterogeneous porous media (i.e., unconsolidated sandpack and Castlegate sandstone) in which we again observed a similar behavior, where two-point correlation functions of 3D pore-space and velocity fields were extremely similar.

## ACKNOWLEDGMENT

This publication was made possible, in part, with the support from National Science Foundation (Grant No. CBET-1604423).

[1] N. S. K. Gunda, B. Bera, N. K. Karadimitriou, S. K. Mitra, and S. M. Hassanizadeh, Lab Chip **11**, 3785 (2011).
[2] M. L. Szulczewski, C. W. MacMinn, H. J. Herzog, and R. Juanes, Proc. Natl. Acad. Sci. USA **109**, 5185 (2012).
[3] S. Osterroth, C. Preston, B. Markicevic, O. Iliev, and M. Hurwitz, Sep. Purif. Technol. **165**, 114 (2016).
[4] W. M. Durham, E. Climent, and R. Stocker, Phys. Rev. Lett. **106**, 238102 (2011).
[5] A. Parmigiani, C. Huber, O. Bachmann, and B. Chopard, J. Fluid Mech. **686**, 40 (2011).
[6] P. K. Kang, M. Dentz, T. Le Borgne, and R. Juanes, Phys. Rev. E **92**, 022148 (2015).
[7] I. Battiato, D. M. Tartakovsky, A. M. Tartakovsky, and T. Scheibe, Adv. Water Resour. **32**, 1664 (2009).
[8] M. J. Blunt, Curr. Opin. Colloid Interface Sci. **6**, 197 (2001).
[9] Y. Zaretskiy, S. Geiger, K. Sorbie, and M. Förster, Adv. Water Resour. **33**, 1508 (2010).
[10] X. Yang, Y. Mehmani, W. A. Perkins, A. Pasquali, M. Schönherr, K. Kim, M. Perego, M. L. Parks, N. Trask, M. T. Balhoff *et al.*, Adv. Water Resour. **95**, 176 (2016).
[11] L. W. Rong, K. J. Dong, and A. B. Yu, Chem. Eng. Sci. **99**, 44 (2013).
[12] W. J. Bosl, J. Dvorkin, and A. Nur, Geophys. Res. Lett. **25**, 1475 (1998).
[13] N. S. Martys, S. Torquato, and D. P. Bentz, Phys. Rev. E **50**, 403 (1994).
[14] Y. Chen, C. Shen, P. Lu, and Y. Huang, Chem. Eng. Process.: Process Intens. **87**, 75 (2015).
[15] C. Zhang, L. Wu, and Y. Chen, Fractals **23**, 1540003 (2015).
[16] S. Ovaysi and M. Piri, J. Comput. Phys. **229**, 7456 (2010).
[17] R. S. Maier, D. M. Kroll, R. S. Bernard, S. E. Howington, J. F. Peters, and H. T. Davis, Phys. Fluids **12**, 2065 (2000).
[18] A. Daneyko, A. Höltzel, S. Khirevich, and U. Tallarek, Anal. Chem. **83**, 3903 (2011).
[19] D. Vidal, C. Ridgway, G. Pianet, J. Schoelkopf, R. Roy, and F. Bertrand, Comput. Chem. Eng. **33**, 256 (2009).
[20] X. Garcia, L. T. Akanji, M. J. Blunt, S. K. Matthai, and J. P. Latham, Phys. Rev. E **80**, 021304 (2009).
[21] C. Pan, M. Hilpert, and C. T. Miller, Phys. Rev. E **64**, 066702 (2001).
[22] R. J. Hill, D. L. Koch, and A. J. C. Ladd, J. Fluid Mech. **448**, 243 (2001).
[23] M. L. Stewart, A. L. Ward, and D. R. Rector, Adv. Water Resour. **29**, 1328 (2006).
[24] J. D. Hyman, P. K. Smolarkiewicz, and C. L. Winter, Phys. Rev. E **86**, 056701 (2012).
[25] P. Gouze, T. Le Borgne, R. Leprovost, G. Lods, T. Poidras, and P. Pezard, Water Resour. Res. **44**, W06426 (2008).
[26] T. Le Borgne, M. Dentz, and J. Carrera, Phys. Rev. Lett. **101**, 090601 (2008).
[27] G. Di Donato, E.-O. Obi, and M. J. Blunt, Geophys. Res. Lett. **30**, 1608 (2003).
[28] M. T. Van Genuchten and P. Wierenga, Soil Sci. Soc. Am. J. **40**, 473 (1976).
[29] R. Haggerty and S. M. Gorelick, Water Resour. Res. **31**, 2383 (1995).
[30] J. H. Cushman and T. R. Ginn, Water Resour. Res. **36**, 3763 (2000).
[31] B. Berkowitz, J. Klafter, R. Metzler, and H. Scher, Water Resour. Res. **38**, 1191 (2002).
[32] G. Srinivasan, D. M. Tartakovsky, M. Dentz, H. Viswanathan, B. Berkowitz, and B. Robinson, J. Comput. Phys. **229**, 4304 (2010).
[33] B. Bijeljic, P. Mostaghimi, and M. J. Blunt, Phys. Rev. Lett. **107**, 204502 (2011).

[34] M. Dentz, P. K. Kang, A. Comolli, T. Le Borgne, and D. R. Lester, Phys. Rev. Fluids **1**, 074004 (2016).
[35] P. de Anna, T. Le Borgne, M. Dentz, A. M. Tartakovsky, D. Bolster, and P. Davy, Phys. Rev. Lett. **110**, 184502 (2013).
[36] B. Bijeljic and M. J. Blunt, Water Resour. Res. **42**, W01202 (2006).
[37] R. S. Maier, D. Kroll, Y. Kutsovsky, H. Davis, and R. S. Bernard, Phys. Fluids **10**, 60 (1998).
[38] Y. E. Kutsovsky, L. E. Scriven, H. T. Davis, and B. E. Hammer, Phys. Fluids **8**, 863 (1996).
[39] M. Siena, M. Riva, J. D. Hyman, C. L. Winter, and A. Guadagnini, Phys. Rev. E **89**, 013018 (2014).
[40] L. Lebon, L. Oger, J. Leblond, J. P. Hulin, N. S. Martys, and L. M. Schwartz, Phys. Fluids **8**, 293 (1996).
[41] M. Icardi, G. Boccardo, D. L. Marchisio, T. Tosco, and R. Sethi, Phys. Rev. E **90**, 013032 (2014).
[42] M. Matyka, J. Gołembiewski, and Z. Koza, Phys. Rev. E **93**, 013110 (2016).
[43] V. A. Patil and J. A. Liburdy, Exp. Fluids **54**, 1497 (2013).
[44] S. S. Datta, H. Chiang, T. S. Ramakrishnan, and D. A. Weitz, Phys. Rev. Lett. **111**, 064501 (2013).
[45] A. J. Chorin, Math. Comput. **22**, 745 (1968).
[46] A. Doostmohammadi, S. Dabiri, and A. Ardekani, J. Fluid Mech. **750**, 5 (2014).
[47] S. Dabiri and G. Tryggvason, Chem. Eng. Sci. **122**, 106 (2015).
[48] O. Botella and R. Peyret, Comput. Fluids **27**, 421 (1998).
[49] T. Suekane, Y. Yokouchi, and S. Hirai, AIChE J. **49**, 10 (2003).
[50] J. Finn and S. V. Apte, Int. J. Multiphase Flow **56**, 54 (2013).
[51] S. Bryant and M. Blunt, Phys. Rev. A **46**, 2004 (1992).
[52] M. Sahimi, *Flow and Transport in Porous Media and Fractured Rock: From Classical Methods to Modern Approaches* (John Wiley & Sons, New York, 2011).
[53] H. Hermann and A. Elsner, Adv. Mater. Sci. Eng. **2014**, e562874 (2014).
[54] M. Skoge, A. Donev, F. H. Stillinger, and S. Torquato, Phys. Rev. E **74**, 041127 (2006).
[55] B. D. Lubachevsky and F. H. Stillinger, J. Stat. Phys. **60**, 561 (1990).
[56] A. R. Kansal, S. Torquato, and F. H. Stillinger, J. Chem. Phys. **117**, 8212 (2002).
[57] R. S. Farr, Powder Technol. **245**, 28 (2013).
[58] S. Torquato and G. Stell, J. Chem. Phys. **77**, 2071 (1982).
[59] M. A. Klatt and S. Torquato, Phys. Rev. E **90**, 052120 (2014).
[60] Z. Deng, X. Liu, C. Zhang, Y. Huang, and Y. Chen, Int. J. Heat Mass Transf. **113**, 1031 (2017).
[61] B. Yu, Appl. Mech. Rev. **61**, 050801 (2008).
[62] R. Hilfer, Phys. Rev. B **45**, 7115 (1992).
[63] G. E. Schröder-Turk, W. Mickel, S. C. Kapfer, M. A. Klatt, F. M. Schaller, M. J. Hoffmann, N. Kleppmann, P. Armstrong, A. Inayat, D. Hug *et al.*, Adv. Mater. **23**, 2535 (2011).
[64] N. Reboul, E. Vincens, and B. Cambou, Granular Matter **10**, 457 (2008).
[65] S. Torquato, *Random Heterogeneous Materials: Microstructure and Macroscopic Properties*, Vol. 16 (Springer Science & Business Media, Berlin, 2013).
[66] S. C. Blair, P. A. Berge, and J. G. Berryman, J. Geophys. Res.: Solid Earth **101**, 20359 (1996).
[67] J. G. Berryman and S. C. Blair, J. Appl. Phys. **60**, 1930 (1986).
[68] S. Torquato, J. Appl. Phys. **58**, 3790 (1985).
[69] Y. Jiao, F. H. Stillinger, and S. Torquato, Phys. Rev. E **76**, 031110 (2007).
[70] H. Okabe and M. J. Blunt, Phys. Rev. E **70**, 066135 (2004).
[71] P. Debye, H. R. Anderson Jr., and H. Brumberger, J. Appl. Phys. **28**, 679 (1957).
[72] J. G. Berryman, J. Math. Phys. **28**, 244 (1987).
[73] O. Rozenbaum and S. R. du Roscoat, Phys. Rev. E **89**, 053304 (2014).
[74] D. Zhang, R. Zhang, S. Chen, and W. E. Soll, Geophys. Res. Lett. **27**, 1195 (2000).
[75] J. Pereira Nunes, B. Bijeljic, and M. Blunt, Water Resour. Res. **52**, 7198 (2016).
[76] B. Bijeljic, A. Raeini, P. Mostaghimi, and M. J. Blunt, Phys. Rev. E **87**, 013011 (2013).
[77] P. Y. Lanfrey, Z. V. Kuzeljevic, and M. P. Dudukovic, Chem. Eng. Sci. **65**, 1891 (2010).
[78] R. Dias, J. A. Teixeira, M. Mota, and A. Yelshin, Sep. Purif. Technol. **51**, 180 (2006).
[79] A. Duda, Z. Koza, and M. Matyka, Phys. Rev. E **84**, 036319 (2011).
[80] M. M. Ahmadi, S. Mohammadi, and A. N. Hayati, Phys. Rev. E **83**, 026312 (2011).
[81] A. Koponen, M. Kataja, and J. Timonen, Phys. Rev. E **54**, 406 (1996).
[82] M. Matyka, A. Khalili, and Z. Koza, Phys. Rev. E **78**, 026306 (2008).
[83] P. Guo, Transp. Porous Media **95**, 285 (2012).
[84] W. Sobieski, Q. Zhang, and C. Liu, Transp. Porous Media **93**, 431 (2012).
[85] J. Comiti and M. Renaud, Chem. Eng. Sci. **44**, 1539 (1989).
[86] B. P. Muljadi, M. J. Blunt, A. Q. Raeini, and B. Bijeljic, Adv. Water Resour. **95**, 329 (2016).
[87] J. Bear, *Dynamics of Fluids in Porous Media* (Courier Corporation, New York, 2013).
[88] P. K. Kang, M. Dentz, T. Le Borgne, S. Lee, and R. Juanes, Adv. Water Resour. **106**, 80 (2017).
[89] H. Tennekes and J. L. Lumley, *A First Course in Turbulence* (MIT Press, Cambridge, MA, 1972).
[90] M. A. Klatt and S. Torquato, Phys. Rev. E **94**, 022152 (2016).
[91] J. S. Andrade, M. P. Almeida, J. Mendes Filho, S. Havlin, B. Suki, and H. E. Stanley, Phys. Rev. Lett. **79**, 3901 (1997).